Structural Characterization and Influence of Defects on the Optical Properties of the Oxygen-Deficient Perovskite Ba3LiNb2O8.5 0.5

Cyrille Galven, Maxime Ducamp, Xavier Rocquefelte, Jens Dittmer, Marie-Pierre Crosnier-Lopez, Françoise Le Berre

Structural characterization and influence of defects on the optical properties of the oxygen-deficient perovskite $Ba_3LiNb_2O_{8.5}\square_{0.5}$

Cyrille Galven[a], Maxime Ducamp[b], Xavier Rocquefelte[b], Jens Dittmer[a], Marie-Pierre Crosnier-Lopez[a] and Françoise Le Berre[a]*

a: Institut des Molécules et Matériaux du Mans (IMMM), UMR CNRS 6283, Le Mans Université, Avenue Olivier Messiaen, 72085 Le Mans Cedex 9, France

b: Institut des Sciences Chimiques de Rennes UMR 6226, Université de Rennes 1, Campus de Beaulieu, 35042 Rennes, France

* : francoise.le-berre@univ-lemans.fr

ABSTRACT

A new oxygen-deficient perovskite $Ba_3LiNb_2O_{8.5}\square_{0.5}$ was synthesized via conventional solid state route and compared to the already known perovskite $Ba_3Li_{0.75}Nb_{2.25}O_9$. The structure of $Ba_3LiNb_2O_{8.5}\square_{0.5}$ was investigated by means of X-ray and neutron diffraction, TEM as well as NMR and XPS spectroscopy. The study of its thermal behaviour revealed an unexpected color change when heated to 1400°C in a sealed platinum tube, with conservation of the initial X-ray structure. First-principles calculations have been performed in order to better understand these observations. The geometry optimizations and the optical spectra simulations highlight the role of both Nb/Li distribution and oxygen-vacancies location.

KEYWORDS

Oxygen-deficient perovskite - powder X-ray and neutron diffraction - TEM - UV-visible spectroscopy - XPS - solid state NMR - DFT calculations

▪ INTRODUCTION

Peroskites represent a family of materials which has been extensively studied for a wide range of attractive properties such as ferroelectricity,[1] piezoelectricity, superconductivity,[2] colossal magnetoresistance,[3] CO_2 capture,[4] or more recently in the field of biomedicine, in which some perovskite nanoparticles are able to bind specifically to cancer cells and thus constitute a new therapeutic perspective.[5] Last but not the least, perovskites are currently under study[6] for their optoelectronic properties and for their interest to produce cheaper and efficient solar cells.

The perovskite family of general formula ABO_3 brings together a very large number of phases with a common structural framework made of corner-sharing BO_6 octahedra. Their arrangement builds 12-fold coordinated cages where the A cations are located. The ideal perovskite has a cubic unit cell (S.G. Pm-3m, Z=1, a_p~4 Å). However, structural distortions (cationic displacement or octahedra tilting) may occur due to steric effects (size of A and B cations) and partial occupancy of the cationic and/or anionic sites. Symmetry lowering thus occurs leading to a wide range of perovskite variants.[7] It must also be noted that the perovskite structure can be encountered with atomic deficiencies on A[8] or oxygen site.[9] Finally, layered perovskites such as Ruddlesden-Popper or Dion-Jacobson, $A'_2[A_{n-1}BnO_{3n+1}]$ and

$A'[A_{n-1}B_nO_{3n+1}]$ (with A, A' = alkaline or alkaline-earth metal and B = metal), are described in the literature.[10,11,12]

In this context, while looking for new lithium phases, we discovered a hitherto unknown perovskite with A = Ba and a mixed occupancy of the B site (2/3 Nb and 1/3 Li). Interestingly, this cationic distribution associated with a perovskite structure implies the existence of oxygen vacancies to preserve the electroneutrality, leading then to the theoretical formulation $Ba_3LiNb_2O_{8.5}\square_{0.5}$. In the literature, a perovskite with the same set of cations but

without oxygen vacancies, $Ba_3Li_{0.75}Nb_{2.25}O_9$, was reported in 1973.[13] This perovskite crystallizes in a cubic cell at Room Temperature (RT) (S.G. Pm-3m, a = 4.095 Å) and presents an irreversible structural transformation above 1300°C from cubic to hexagonal symmetry (S.G. $P6_3/mmc$, a = 5.803 Å and c = 19.076 Å) due to a partial Li and Nb ordering.[14]

Herein, we propose to characterize the perovskite phase $Ba_3LiNb_2O_{8.5}\square_{0.5}$ with a special attention to the effect of the presence of oxygen vacancies. Its structural determination is based on the combination of a wide range of experiments (X-ray and neutron diffraction, transmission microscopy, DTA, NMR and XPS spectroscopy) and theoretical calculations based on Density Functional Theory (DFT). Finally, the optical properties evolution upon heating was investigated from both UV-visible spectroscopy and theoretical simulations.

▪ EXPERIMENTAL SECTION

Synthesis. $Ba_3LiNb_2O_{8.5}\square_{0.5}$ and $Ba_3Li_{0.75}Nb_{2.25}O_9$ samples were synthesized by using conventional solid state route between stoichiometric amount of dried Li_2CO_3 (sigma Aldrich, 99%), $BaCO_3$ (prolabo, 99.5%) and Nb_2O_5. This last oxide was prepared by dehydration of $HNbO_3$ at 600°C for 15 min, the $HNbO_3$ compound being prepared according to the procedure described by Rice and al.[15] The mixtures were then pelletized and heated at 900°C for 12 hrs.

To improve the crystallinity of the samples, powders were introduced in platinum tubes after the synthesis and dried under vacuum at 150°C over night. Tubes were then sealed by arc melting and heated at 1400°C for 12 hrs.

For all heat treatments, a natural cooling of the furnace was applied.

Powder Diffraction Experiments. The Powder X-ray Diffraction (PXRD) data of $Ba_3LiNb_2O_{8.5}\square_{0.5}$ and $Ba_3Li_{0.75}Nb_{2.25}O_9$ were collected in air with a PANalytical X'pert Pro

diffractometer equipped with the X'Celerator detector using Co Kα radiation. The data were collected in the 5–130° 2θ range with a 0.017° step and a counting time of 220 seconds per step.

The Powder Neutron Diffraction (PND) data were recorded at ILL Grenoble on the D2B high resolution neutron diffractometer for $Ba_3LiNb_2O_{8.5}\square_{0.5}$ prepared at 900°C (λ = 1.594678 Å; angular range (°2θ) = 0.05-159.95; step scan increment (°2θ) = 0.05; counting time = 4 h). For $Ba_3LiNb_2O_{8.5}\square_{0.5}$ heated at 1400°C in a sealed platinum tube, the data have been recorded on the 3T2 instrument at the LLB Saclay (λ = 1.228917 Å; angular range (°2θ) = 4.50-120.45; step scan increment (°2θ) = 0.05; counting time = 4 h)

Treatment of all diffraction data was carried out by the Rietveld method[16] using Fullprof software[17] with a pseudo-Voigt function to describe the peak shape. The background level was determined manually before being refined.

Transmission Electron Microscopy (TEM). The TEM study on $Ba_3LiNb_2O_{8.5}\square_{0.5}$ was performed on a JEOL JEM 2100 HR electron microscope operating at 200 kV and equipped with a side entry ± 35° double-tilt specimen holder. To promote random orientation of crystallites, the samples were ultrasonically dispersed in ethanol and one drop of this suspension was deposited onto a holey carbon-coated copper grid before a final air drying.

X-ray Photoelectron Spectroscopy (XPS). The XPS measurements were carried out with a Kalpha ThermoFisher Scientific using Al radiation (hν = 1486.6 eV) on $Ba_3LiNb_2O_{8.5}\square_{0.5}$ powder sample heated at 1400°C in a sealed platinum tube. No Ar etching was used prior to data acquisition so as not to induce a niobium reduction as already reported in the literature.[18] The X-ray spot size is 200 μm and the analysed depth is between 3 and 5 nm. In such conditions, all atoms with a Z number greater than or equal to 3 are detected as long as their content is at least 0.2% at.

Solid-state NMR. All NMR experiments have been performed on a Bruker 300 WB spectrometer operating at a magnetic field of 7 T. ^{7}Li spectra have been acquired as one-pulse experiments on a 1.3 mm dual channel probe under 40 kHz magic angle spinning (MAS). 8 scans were accumulated, the recycle delay was 300 s. ^{93}Nb experiments were done as Hahn echo experiments with the same probe under 60 kHz MAS. 160 K scans were accumulated, the recycle delay was 200 ms. Another set of ^{93}Nb experiments was performed under static conditions as WURST-QCPMG on a 2.5 mm dual channel VTN probe. Non-adiabatic WURST pulses of 200 μs with a nominal sweep width of 1 MHz and identical excitation and refocusing power were applied. The total echo time was 440 μs; 16 echoes were acquired and co-added. Spectral uniformity of the excitation and refocusing was improved by adding spectra with both high-to-low and low-to-high frequency sweep pulses. As the actual range of excitation uniformity was 500 kHz (limited by circuitry and/or pulses), a combination of three spectra with carrier steps of 300 kHz was used to ensure there was no spectral distortion in the range of interest and to enhance this range. The three partial spectra exhibit a continuous transition and were combined to the total spectra shown.

Optical measurements (UV−Visible−Near-Infrared Spectroscopy). UV−vis diffuse reflectance spectra were recorded at room temperature from 300 to 1000 nm with a 1 nm step, using a Shimadzu UV-2700 spectrophotometer. The 100% reflectance was obtained with a Halon powder reference. The reflectivity spectra (R) were transformed into the absorption α/S spectra using a Kubelka−Munk transformation.

Density Functional Theory (DFT) calculations. All calculations were carried out within the Density Functional Theory (DFT) as implemented in the Vienna *ab initio* Simulation Package (VASP).[19,20,21] For electron exchange and correlation we used the Generalized Gradient approximation as parameterized by Perdew, Becke, and Ernzehof (PBE)[22,23] and the meta-GGA SCAN functional. Atom cores are described through the projector augmented wave

(PAW) method.[24, 25] The kinetic energy cutoff for plane wave expansions was set to 500 eV, and the Brillouin zone was sampled by Monkhorst–Pack meshes.[26] Atomic positions were optimized until forces were converged to lower than 3.10^{-2} eV/Å. DOS were shifted so that the Fermi level lies at 0 eV. The presence of defects (oxygen vacancies) and the Nb/Li distribution have been considered using a supercell approach. Two different models have been envisioned with hexagonal and tetragonal symmetries, respectively. More details about the construction of these models are provided in the discussion.

▪ RESULTS AND DISCUSSION

Characterization at RT (PXRD, PND and TEM)

In this first part, we discuss the structural characterization at room-temperature of $Ba_3LiNb_2O_{8.5}\square_{0.5}$ sample in comparison to $Ba_3Li_{0.75}Nb_{2.25}O_9$ using X-ray/neutron diffraction and TEM technique. The color of the two perovskite phases after the synthesis at 900°C was slightly different: $Ba_3Li_{0.75}Nb_{2.25}O_9$ was white whereas $Ba_3LiNb_2O_{8.5}\square_{0.5}$ was light beige. These compounds are noted hereafter in the paper respectively as White-O_9 and Beige-$O_{8.5}$. PXRD patterns were essentially identical (Figure 1) with relatively wide *hkl* lines for the two perovskites indicating a low crystallinity.

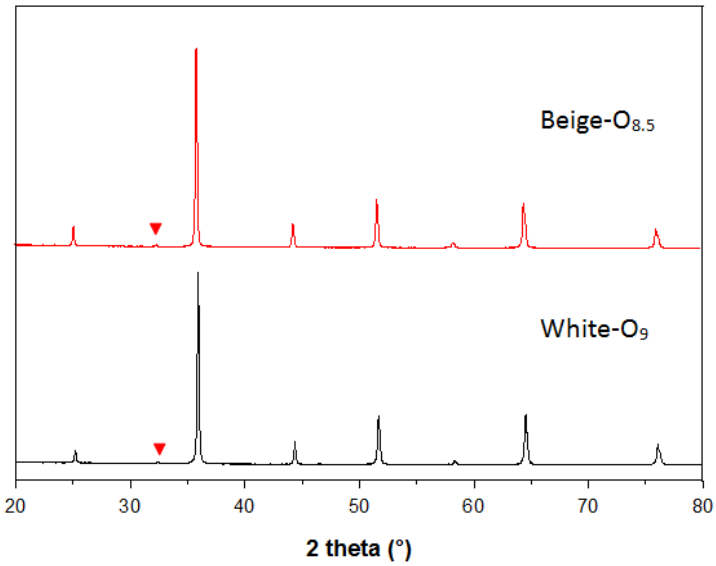

Figure 1 : PXRD patterns of $Ba_3Li_{0.75}Nb_{2.25}O_9$ and $Ba_3LiNb_2O_{8.5}\square_{0.5}$ (▼: K_β) respectively quoted as White-O_9 and Beige-$O_{8.5}$

According to ref 13, all the lines for both compounds have been indexed in the cubic Pm-3m space group (n°221) with very close cell parameters (Table 1) confirming thus the purity of each sample and meaning that there is no ordering between lithium and niobium cations visible by PXRD.

Table 1: Color and cell parameter (Å) of $Ba_3Li_{0.75}Nb_{2.25}O_9$ and $Ba_3LiNb_2O_{8.5}\square_{0.5}$

	x = 0	x = 0.25
Formulation	$Ba_3Li_{0.75}Nb_{2.25}O_9$	$Ba_3LiNb_2O_{8.5}\square_{0.5}$
Synthesized at 900°C	White - 4.1082(2)	Light beige - 4.1085(2)
After annealing at 1400°C in Pt tube	White a_c = 4.11434(6) a_{hexa} = 5.79941(6); c_{hexa} = 19.0668(2)	Purple – 4.10731(6)

The well-known Goldschmidt tolerance factor (t) [27] of the ABO_3 perovskite structure characterizes the influence of the ionic radii on the symmetry. Usually, a hexagonal symmetry is preferred if t is over 1.05, while for $1 < t < 1.05$ a cubic symmetry is expected. For smaller t values, tetragonal ($0.97 < t < 1.0$) or orthorhombic/monoclinic ($t < 0.97$) distortions are

observed. [28] Here, the ionic radius for the Nb/Li cations was calculated based on the proportion of Nb and Li cations in the B site for each compound. For White-O_9 and Beige-$O_{8.5}$, the so-obtained *t* values are, respectively, 1.03 and 1.04, which corresponds to the domain where the cubic symmetry is preferred, in good agreement with the PXRD results.

To ensure that the two compounds are effectively different, structural refinements were performed from PXRD data by considering the two chemical formulations $Ba_3Li_{0.75}Nb_{2.25}O_9$ and $Ba_3LiNb_2O_{8.5}$ as possible for the two compounds. Due to the different niobium quantity in the two formulations, it should be possible to differentiate $Ba_3Li_{0.75}Nb_{2.25}O_9$ from $Ba_3LiNb_2O_{8.5}\square_{0.5}$ from PXRD data. As shown in Table 2, better reliability factors are obtained with the chemical formulations $Ba_3Li_{0.75}Nb_{2.25}O_9$ and $Ba_3LiNb_2O_{8.5}\square_{0.5}$, respectively for White-O_9 and Beige-$O_{8.5}$.

Table 2 : Reliability factors for refinements of White-O_9 and Beige-$O_{8.5}$

White-O_9

Refined as $Ba_3Li_{0.75}Nb_{2.25}O_9$	Rp = 6.91	Rwp = 7.32	Rexp = 3.75	chi² = 3. 08	R_B = 1.63
Refined as $Ba_3LiNb_2O_{8.5}$	Rp = 11.3	Rwp = 13.3	Rexp = 5.93	chi² = 5.03	R_B = 8.87

Beige-$O_{8.5}$

Refined as $Ba_3LiNb_2O_{8.5}$	Rp = 7.51	Rwp = 7.67	Rexp = 3.94	Chi² = 3. 78	R_B = 1.71
Refined as $Ba_3Li_{0.75}Nb_{2.25}O_9$	Rp = 12.3	Rwp = 13.1	Rexp = 3.75	chi² = 12.2	R_B = 9.69

As neutron diffraction is more sensitive for the location of light atoms, a complete structural refinement for Beige-$O_{8.5}$ with neutron data was then undertaken, to confirm the presence of oxygen vacancies, the Nb/Li ratio (2/1) and to check if there was a superstructure not detected by PXRD. With this neutron data set, we observed that all the *hkl* lines could be indexed in the simple cubic cell deduced from the PXRD study (S.G. Pm-3m) (Figure 2). This means that the octahedra are regular and not tilted, otherwise additional *hkl* lines, corresponding to a larger cell, would be observed. It can also be noted on this figure that no obvious diffuse scattering in the background is observed.

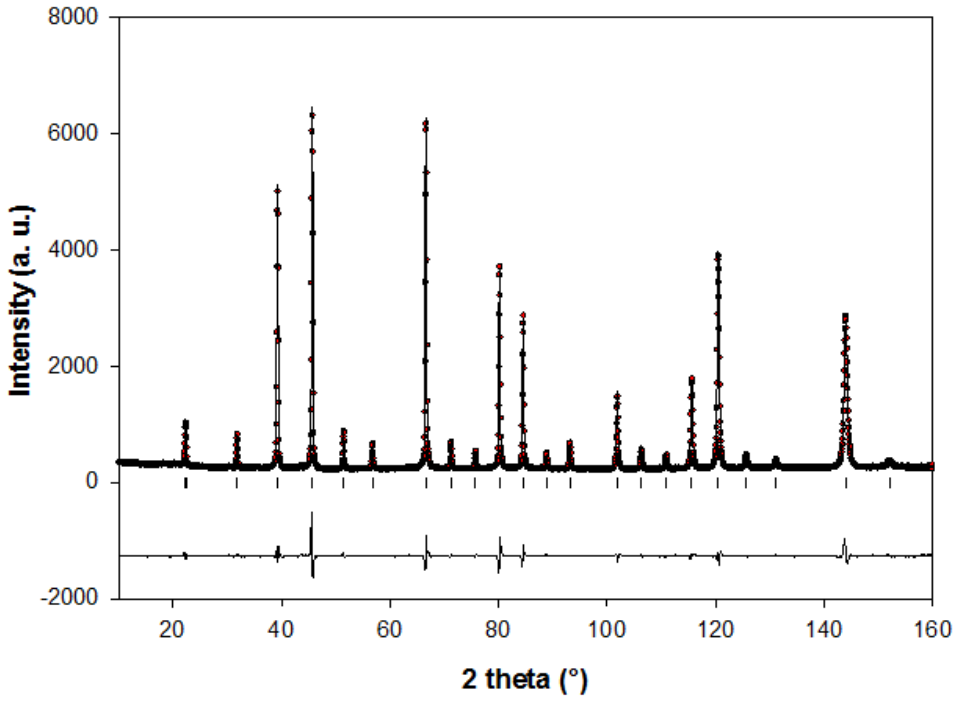

Figure 2: Observed, calculated and difference PND patterns of Beige-$O_{8.5}$ synthesised at 900°C (S.G.: Pm-3m). Vertical bars are related to Bragg reflection positions.

The structural refinements were carried out with the classical perovskite model in the Pm-3m space group: one crystallographic site for each kind of atom (1b for Ba, 1a for Nb and Li and 3d for O) and one isotropic displacement factor for each site. The oxygen site occupancy rate was refined as well as the Nb/Li ratio with a condition of full site occupancy. The refinement converged quickly towards good reliability factors and to the chemical formulation $Ba_3Li_{0.96(1)}Nb_{2.04(1)}O_{8.48(5)}$, confirming thus the presence of oxygen vacancies. This formulation almost respects the necessary electroneutrality: 17.16 positive charges versus 16.96 negative charges. Table 3 gathers the cell parameters and the refined profile parameters for the PND data. Atomic coordinates, isotropic thermal parameters and bond valence sums are reported in Table 4 with selected interatomic distances. A refinement with anisotropic displacement parameters has been carried out but did not reveal any particular atomic motion and did not improved the results.

Table 3: Structure refinement results of Beige-$O_{8.5}$ from PND data in the Pm-3m S.G.

	Beige-$O_{8.5}$
Space group	Pm-3m
Cell parameter (Å)	4.10733(3)
R_p	10.6
R_{wp}	10.6
R_{exp}	3.18
χ^2	11.0
Bragg R-factor	1.33
η	0.33(2)
Half-width parameters:	
u	0.074(2)
v	-0.082(4)
w	0.093(2)

Table 4: Atomic coordinates, B_{iso} (Å^2), bond valence sums (Σv) and selected interatomic distances (Å) for Beige-$O_{8.5}$ from PND data in the Pm-3m S.G.

Atom	site	x	y	z	B_{iso}(Å^2)	sof	Atoms number	Σv	$\Sigma v_{expected}$
Ba	1b	0.5	0.5	0.5	0.70(3)	1	3	2.1	2
Nb	1a	0	0	0	0.21(3)	0.681(4)	2.04(1)	3.9	5
Li	1a	0	0	0	0.21(3)	0.319(4)	0.96(1)	1.2	1
O	3d	0.5	0	0	1.07(2)	0.942(6)	8.48(5)	1.8	2
Distances: Nb/Li-O : 6 × 2.0537 ; Ba-O : 12 × 2.9043									

As for all simple 3D cubic perovskites, the Beige-$O_{8.5}$ structure is constituted of corner-sharing regular BO_6 octahedra, the B site being statistically occupied by two thirds of Nb and one third of Li. If we consider such a Li/Nb statistical occupancy and the ionic radii of Nb^{5+} (0.64 Å) and Li^+ (0.76 Å), taken in an octahedral environment from the Shannon table,[29] we

obtain an effective ionic radius of 0.68 Å for the B cation. It leads to an expected B-O distance close to 2.03 Å, not very far from the observed one (2.0537 Å). We can note that the partial occupation of the oxygen site (94.4%) means that the B cations can be locally surrounded by less than 6 O^{2-} anions. To go further, we have estimated the bond valence sums (BVS)[30] using R_0 values of 2.290, 1.911 and 1.466 for Ba^{2+}, Nb^{5+} and Li^{+} ions respectively, and taking into account the partial occupancy of the oxygen site. The A site of the perovskite structure is fully occupied by Ba^{2+} cations (Ba-O distance of 2.9043 Å) leading to a BVS value of 2.1, close to the expected value of 2.0. Concerning the B site, either occupied by Li^{+} or Nb^{5+} ions, the BVS values obtained for an octahedral environment are 1.2 and 3.9 for Li^{+} and Nb^{5+} ions. These values significantly deviate from the expected ones (1.0 and 5.0 for Li^{+} and Nb^{5+} ions respectively). This can be explained by the statistical occupancy of the B site leading consequently to B-O distances values intermediate between Nb-O and Li-O distances reported in the literature (Li^{+} has a larger radius than Nb^{5+}). It leads to a too large (too small) site for Nb^{5+} ions (Li^{+} ions) and thus a smaller (larger) BVS value. However, for the Li^{+} ions, the 1.2 BVS value could be due in addition to a preferential localization of O^{2-} vacancies around this cation. To check that these anomalous BVS values are due to the statistical occupancy, we have analysed the optimized geometries of three models (noted H1, H2 and H3 in DFT calculations part) which differ by the Li/Nb ordering. In the 3 cases, the BVS values of Li and Nb are, respectively, 1.0 and 4.7 after the geometry optimization. It confirms that after relaxing locally the environment around both cations, the BVS values agree with the expected ones.

To complete this structural part, a TEM study was performed on Beige-$O_{8.5}$. In addition to the intense reflections related to the cubic cell, weak diffuse scattering signals have been observed on some diffraction patterns (Selected Area Electron Diffraction mode), and High Resolution Electron Microscope (HREM) images showed irregular contrasts (Figures S1 and

S2). These observations suggested a local ordering Nb/Li and/or vacancies/O, without being able to clearly identify the origin.

Temperature behaviour study of Beige-$O_{8.5}$ and White-O_9.

To improve the crystallinity of both samples, an annealing at high temperature was performed. For this, the compounds were placed in a sealed platinum tube before being heated 12 h at 1400°C to prevent a possible lithium volatilization as frequently observed with lithium oxides. This temperature was chosen not only to effectively improve the crystallinity but also to check the existence of a hexagonal form for $Ba_3LiNb_2O_{8.5}\square_{0.5}$ as observed for $Ba_3Li_{0.75}Nb_{2.25}O_9$ in ref 14.

The PXRD patterns recorded after the heating revealed thinner *hkl* lines for both compounds, confirming an improved crystallinity (Figure S3). For Beige-$O_{8.5}$ we observed the preservation of the cubic cell with similar refined cell parameters (Table 1). For White-O_9, the PXRD pattern was completely different indicating that the structural transition previously mentioned in ref 14 has occurred (Figure S4). Indeed, most of the *hkl* lines could be indexed in the hexagonal cell (S.G. $P6_3/mmc$) while the remaining ones correspond to the cubic variety.

In addition to the improvement of the crystallinity, we observed that surprisingly, the color of Beige-$O_{8.5}$ turned to pink (sample termed hereafter Pink-$O_{8.5}$) (Figure 3) while White-O_9 remained white.

Figure 3: $Ba_3LiNb_2O_{8.5}\square_{0.5}$ before and after the annealing at 1400°C in a sealed platinum tube showing the change in color, Beige-$O_{8.5}$ (left) and Pink-$O_{8.5}$ (right)

Given this significant color change, a new complete structural determination was undertaken on Pink-$O_{8.5}$ sample from PND data (Figure S5). An identical structure to that of Beige-$O_{8.5}$ was obtained indicating that no structural modification, from the viewpoint of PND, has occurred during the heating step in platinum tube (Tables S1 and S2).

The TEM study performed on this sample revealed, as for Beige-$O_{8.5}$, additional diffuse reflections and inhomogeneous contrast in high resolution images (figure S6).

XPS experiments were then performed on the Pink-$O_{8.5}$ sample in order to check if the color's change was due to a partial reduction of the niobium cations during the annealing at 1400°C. Spectral lines of Nb $3d_{3/2}$ and Nb $3d_{5/2}$ are represented in Figure S7. The observed signals are consistent with the presence of only Nb^{5+}, since a partial niobium reduction (Nb^{3+} or Nb^{4+}) would imply additional signals at lower energy[18] (≈ 203.5 eV for Nb^{3+} and ≈ 205 eV for Nb^{4+}). As it could be argued that only a tiny portion of niobium, not detectable by XPS, was reduced, we have then performed Electron Paramagnetic Resonance (EPR). Indeed, Nb^{4+} ion has a $4d^1$ electronic configuration, and we must be able to detect it if present in the samples. X-band EPR experiments were performed which have a sensitivity of about 10^{12} spins/g, *i.e.* a $[Nb^{4+}]/[Nb]$ ratio of about 5×10^{-10} for the studied compounds. However, no EPR signal, characteristic of Nb^{4+} ions, has been detected, this excluding that the color change is due to a partial reduction of some Nb^{5+} ions. This point concerning the color change is discussed later in the DFT section.

Solid-state NMR

NMR experiments were performed to probe the differences in the local environment between Beige-$O_{8.5}$ and Pink-$O_{8.5}$ and the changes with respect to White-O_9, which has no oxygen vacancy. Figure 4a shows the ^{7}Li MAS spectra of the three samples.

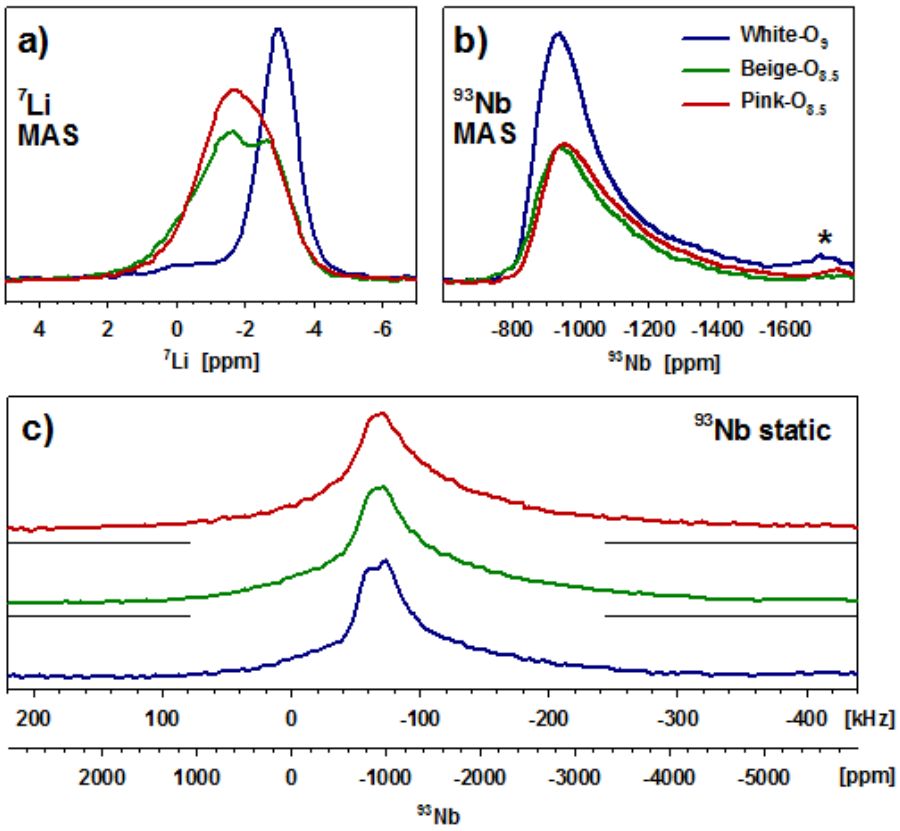

Figure 4 : NMR spectra of materials White-O_9 (blue), Beige-$O_{8.5}$ (green), and Pink-$O_{8.5}$ (red). (a) ^{7}Li, 40 kHz MAS. (b) ^{93}Nb, 60 kHz MAS. The asterisk denotes the first spinning sideband. (c) ^{93}Nb, static, scaled to the same maximum.

Apart from a broad foot of unclear origin, a single resonance at -2.95 ppm is observed in White-O_9, confirming the presence of a single Li site. In contrast, the ^{7}Li signal of Beige-$O_{8.5}$ shows two maxima, one of them having a resonance frequency (-2.8 ppm) close to that of White-O_9. The new partial signal at -1.6 ppm is thus interpreted as stemming from undercoordinated lithium in the samples containing oxygen vacancies, i.e. most probably five-fold coordinated Li. It is broader, reflecting the higher degree of disorder due to the vacancies. Also the signal of Pink-$O_{8.5}$ appears to consist of these two resonances, with either different populations, signal positions or widths (disorder).

^{93}Nb spectra have been acquired in static mode and under MAS (Figure 4b and 4c). The static ^{93}Nb spectra show the central transition (Figure 4c), which is however so broad that it has to

be composed of three spectra acquired with frequency modulated broadband pulses at three different carriers (see Experimental for details). Already the signal of White-O_9 shows a shape that is typical for a broader distribution of quadrupolar coupling due to disorder, albeit some residual features of 2nd order quadrupolar coupling line shapes can be recognized. The spectrum of the same compound under MAS, with a much better resolution, confirms that these features are not due to two different sites (Figure 4c). The disorder is due to the statistical Nb/Li distribution in the second cation neighbour of the niobium.[31] The static ^{93}Nb spectra of the two vacancy phases are qualitatively similar, while the above features are broadened out by the additional disorder introduced by the vacancies. This is also visible in the ^{93}Nb MAS spectra. However, while the quadrupolar coupling, essentially already showing an almost fully disordered signal, is not able to identify a five-fold coordination, the chemical shift would be able to do so. The signal maximum of about -940 ppm corresponds to the upper limit of the chemical shift range of 6-fold oxygen coordinated niobium (including the isotropic quadrupolar shift).[32] It would also match a 5-fold coordination, however, a change of a non-negligible part of the cations to a five-fold coordination should be reflected in the spectra by a second signal further downfield (as seen for ^{7}Li) or at least a broadening into that direction. A slight broadening is observed, however upfield, and it can be explained by the quadrupolar coupling. One explanation for the discrepancy to the Li spectra would be that the oxygen vacancies are situated between two lithium cations (hypothesis 1). This interpretation would also explain the relatively high 5-coordinated Li signal. Another possibility would be that the higher asymmetry of a five-fold Nb coordination increases the quadrupolar coupling so that these ^{93}Nb signals are, in combination with disorder, broadened beyond detectability (hypothesis 2). These two hypotheses will be discussed in the analysis of the DFT calculations part.

Before discussing the theoretical results, let's first summarize the main conclusions arising from the experimental investigations. NPD confirms oxygen vacancies in both $Ba_3LiNb_2O_{8.5}\square_{0.5}$ samples while TEM suggests a local ordering Nb/Li and/or vacancies/O. Concerning the NMR, it shows multiple environments for Li but is less conclusive for Nb. The following theoretical investigation has thus two main objectives : the first one concerning the structural characterization and the second one related to the understanding of the optical properties.

Structural characterization based on DFT calculations

In order to investigate the effects of the Li/Nb and oxygen-vacancy distributions on the atomic and electronic structures, we have realized DFT calculations by generating 2 types of models, both leading to the chemical formulation $[Ba_6Li_2Nb_4O_{18}]^{2-}$. A point defect must be added to have charge neutrality. Here, it corresponds to one oxygen vacancy, thus leading to the formulation $Ba_6Li_2Nb_4O_{17}\square_1$, which corresponds to the composition of the new perovskite studied in this article. The first model is based on the hexagonal cell (Figure S8), with a doubling of c_1. The second model is based on a tetragonal ($a\sqrt{2} \times a\sqrt{2} \times 3a$) supercell (with *a*, the cubic cell parameter). Both contain 4 Nb and 2 Li, but while the hexagonal cell is based on 6 slabs, the tetragonal one is based on 3 slabs. For that reason, the hexagonal supercell has been used to probe the effect of the Nb/Li distribution and the vacancy position, while the tetragonal cell was used to probe the effect of the concentration of oxygen vacancies.

In the hexagonal model, 3 Li/Nb orderings have been envisioned, noted H1, H2 and H3 (Figure 5). One way to distinguish these three models is to consider the shortest Li-Li distance which increases from H1 to H3.

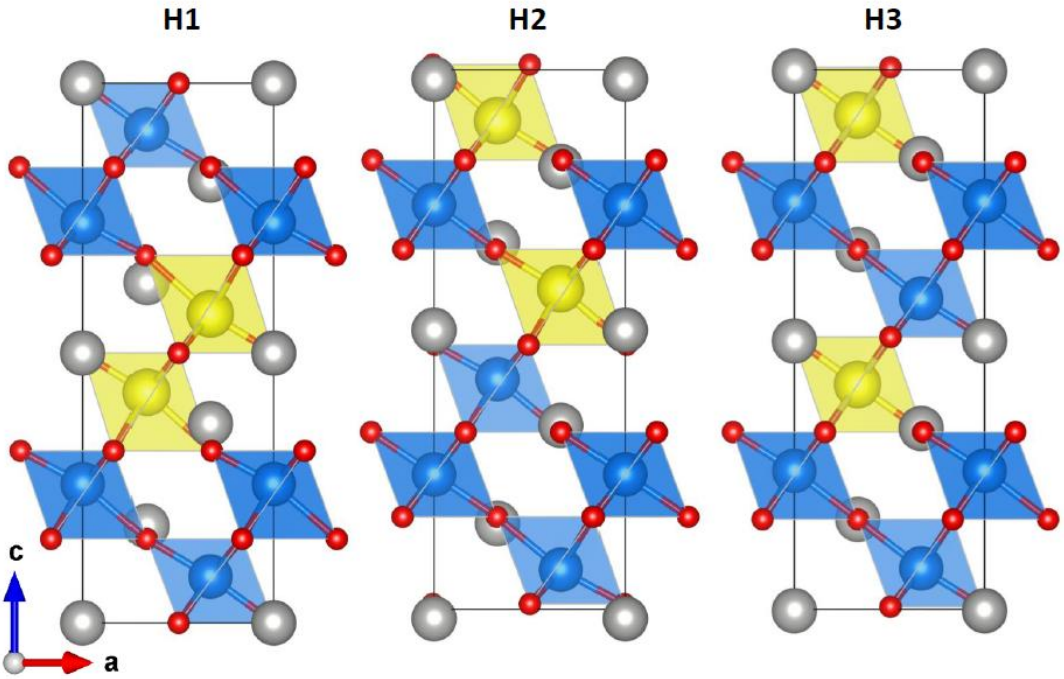

Figure 5 : Schematic representation of the optimized geometries of the 3 theoretical models based on a hexagonal supercell (H1, H2 and H3), using meta-GGA SCAN functional. Lithium, niobium, barium and oxygen atoms are represented in yellow, blue, grey and red. The octahedra NbO_6 and LiO_6 are represented in blue and yellow. These three models are without oxygen vacancy and differ by the Li/Nb ordering. The charge neutrality was assumed by imposing a homogeneous background charge.

Before creating an oxygen vacancy, we have performed geometry optimization of these three models, by including a background charge to ensure the charge neutrality. The resulting relative energies evidenced that the H3 model is significantly more stable than the two other ones, with 4.6, 0.8 and 0 eV for H1, H2 and H3, respectively (H3 taken as the reference energy). It evidences that the Li/Nb distribution strongly impacts the stability of the system, with a preference to situations avoiding short Li-Li distances. H3 corresponds to the most homogeneous distribution of Nb^{5+} and Li^{+} in such a hexagonal supercell, with a succession of 2 Nb-layers and 1 Li-layer in all directions, allowing to minimize the Madelung energy. It is also interesting to notice that the band gap increases from H1 to H3. H1, the less stable model is metallic and H2 and H3 semiconductors with E_g = 1.9 and 3.3 eV, respectively (Figure 6).

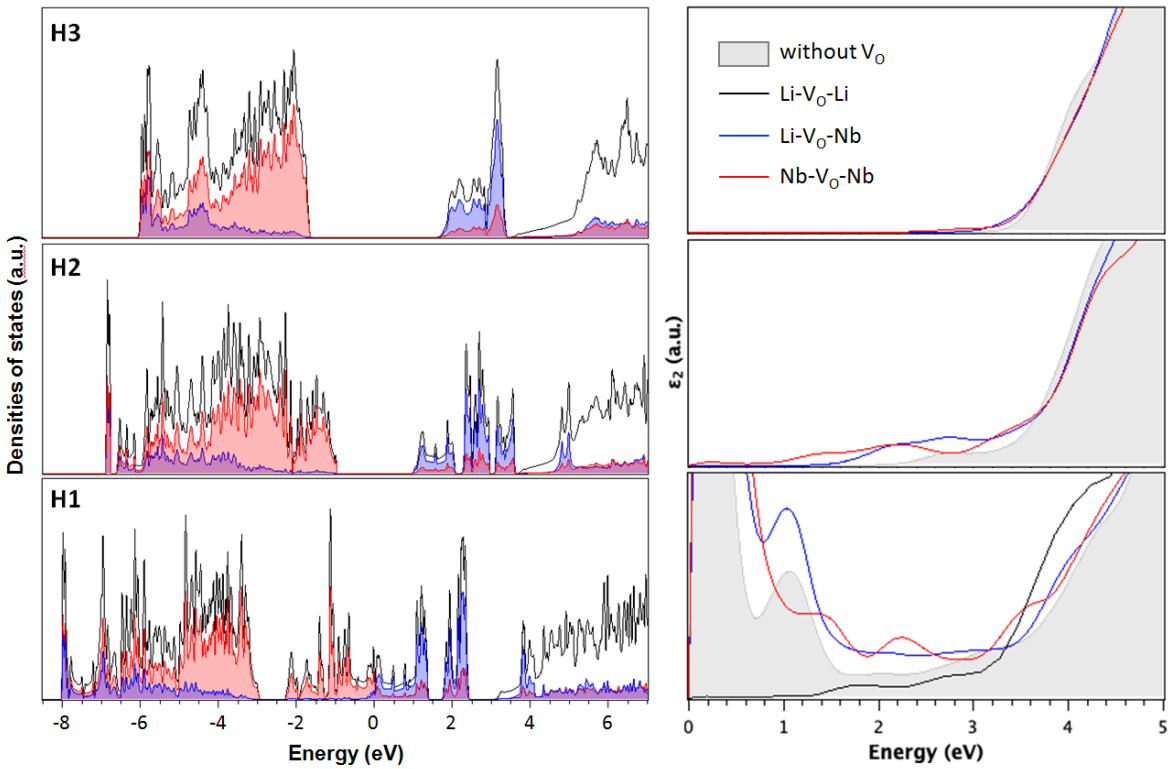

Figure 6 : Densities of states (DOS) of models without oxygen vacancy (left) and simulation of the optical properties of models (right) with or without oxygen vacancy. Total DOS are represented in black and partial DOS of oxygen and niobium in red and blue, respectively. The Fermi level is defined as the reference of energies. The optical properties of the models without oxygen vacancy are shown in grey and the ones with oxygen vacancy in black, blue and red, for an oxygen vacancy Li-V_O-Li, Li-V_O-Nb and Nb-V_O-Nb, respectively.

The next step is to consider the impact of the oxygen vacancy for these 3 Li/Nb orderings in the hexagonal model. The notation will be $H_x[1V_O]$ with x = 1, 2 or 3 and $1V_O$ to specify that one oxygen vacancy has been created. All oxygen atoms have two cation neighbours (corner sharing octahedra), thus leading to three types of oxygen vacancies (V_O), i.e. Nb-V_O-Nb, Li-V_O-Nb and Li-V_O-Li. The latter is only possible with H1. Seven oxygen vacancy systems have thus been generated. Their relative energies, after geometry optimization, are represented as function of the Li-Li distance in Figure 7.

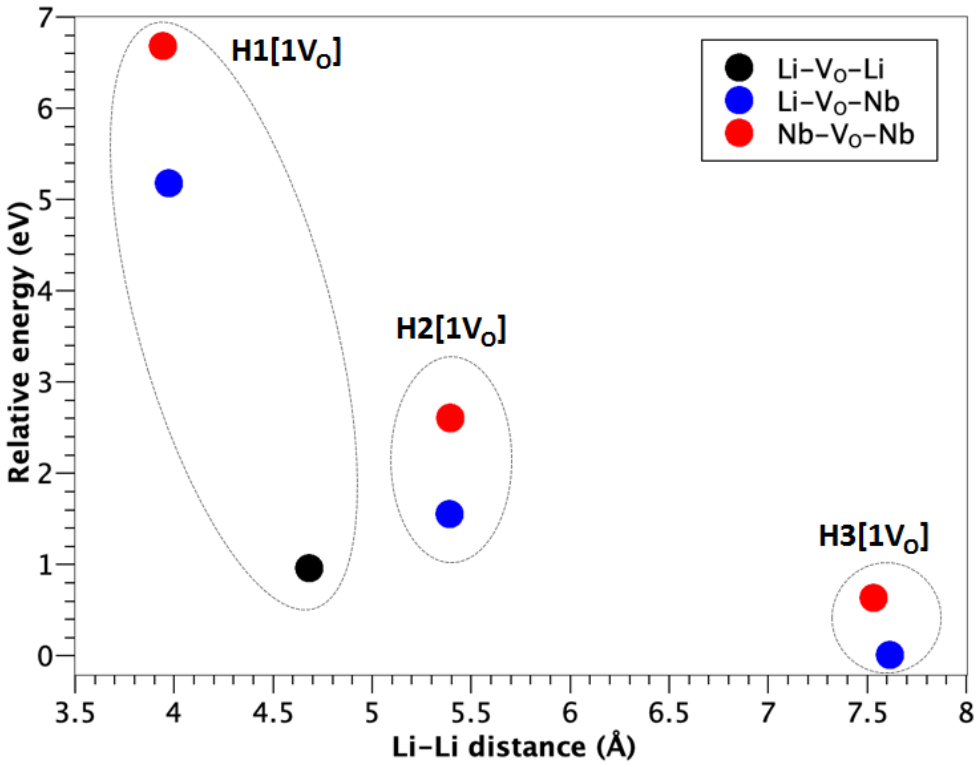

Figure 7 : Relative energies of the oxygen vacancy models as function of the Li-Li distance. The most stable structure, i.e. H3[1V_O] with an oxygen vacancy between Nb and Li, has been chosen as the reference of energies. Li-V_O-Li, Li-V_O-Nb and Nb-V_O-Nb correspond to oxygen vacancies between 2 Li, Li and Nb, and 2 Nb atoms, respectively

It shows some systematic features. Creating an oxygen vacancy between one Nb^{5+} and one Li^+ (blue circle) is more favourable than between two Nb^{5+} ions (red circle), with an energy difference of 1.5, 1.1 and 0.6 eV for H1, H2 and H3, respectively. In the case of H1, it is also possible to create an oxygen vacancy between two Li^+ ions. This calculation (black circle), among the H1[1V_O] models, leads to the lowest energy, i.e. 4.2 and 5.7 eV lower in energy than Li -V_O- Nb and Nb-V_O-Nb, respectively, matching to hypothesis 1 for the absence of a second Nb^{5+} NMR signal. In summary, the most stable system remains H3[1V_O] with Li-V_O-Nb. However, H1[1V_O] with Li-V_O-Li is significantly stabilized, strongly reducing the energy difference between these two models from 4.6 to 1.0 eV, when V_O is created. It means then that oxygen vacancies will preferentially form between two Li^+ ions, if such a situation occurs in the compound, then between Li^+ and Nb^{5+}, and finally between two Nb^{5+} ions.

Optical properties from DFT calculations

Figure 6 shows, in addition to Densities Of States (DOS) of H1, H2 and H3 (without V_O), the related optical spectra (in grey). The optical properties are described considering the imaginary part of the dielectric function (ε_2), which characterizes the photon absorption. The evolution of the optical properties after creating one oxygen vacancy are represented using black, blue and red plain lines for Li-V_O-Li, Li -V_O- Nb and Nb-V_O-Nb, respectively. Before discussing the effect of V_O, let us discuss the impact of Li/Nb distribution on the optical properties of H1, H2 and H3 models. As mentioned above, the band gap increases from H1 to H3, as evidenced in the DOS, which is mainly constituted of O(2p) states in the Valence Band (VB) and Nb(4d) states in the Conduction Band (CB). While the Nb(4d) band is clearly empty in H2 and H3 calculations, it is slightly occupied in H1 due to its metallic character. Looking at the projected DOS (pDOS) of H1 (Figure 6), it appears that the states at the Fermi level (E_F) are related to the oxygen connecting the two Li^+ ions. It is interesting to notice that this oxygen does not interact with niobium, and only H1 shows this feature. The pDOS shows no overlap between Li and O states, confirming the ionic character of the bond, but evidences an overlap between Ba and O states. And, indeed, shorter Ba-O distances in this region of 2.5 Å are obtained in our calculations, compared to the more stable H3 model where the Ba-O distances are about 2.9 Å. One simple explanation is the necessity to compensate the high concentration of Li^+ ions in H1, which leads to strong deficiency of positive charges in the compound (electrostatic screening). Interestingly, removing this oxygen leads to the most stable H1[1V_O] model (Figure 7). The two others, by keeping this oxygen, remain metallic as evidenced in the simulations of the optical absorption properties (blue and red curves). In contrast, H1[1V_O] with Li-V_O-Li exhibits semi-conductive properties (black curve) with an optical gap of about 1.2 eV. The two other systems and their V_O-derivatives show semi-

conductive properties. In the case of H3, the optical properties are nearly unchanged when creating an oxygen vacancy, with an optical band gap of about 3 eV. In contrast, significant evolutions are observed in the ε_2 simulations when V_O is created in H2, with an optical band gap going from 2.2 eV (without V_O) to 1.4 and 0.8 eV for Li -V_O- Nb and Nb-V_O-Nb, respectively. To summarize this part, it clearly appears that two levers can be envisioned to tune the optical properties of the system: (1) the Li/Nb distribution and (2) the oxygen vacancies position. Neglecting the metallic models (highly unstable), optical absorptions in the visible range are found for H1 (with Li-V_O-Li), H2 (with Li -V_O-Nb) and H2 (with Nb-V_O-Nb). It should be noted that their intensity remains small, and indeed the pink color of our samples is faint. However, the fact that the color of the powder changes upon heating, without changing the X-ray diagram (except a better crystallinity), could be explained by a core-shell model, with the idea that the defects could migrate from the inner to the outer of the particle.

To test the idea that a higher concentration of vacancies in the shell could explain the change of optical properties, we have used the tetragonal model presented before, noted T1, leading to a lowering of symmetry from Pm-3m to $P4_2/nmm$. From T1, we have created one V_O, noted T1[1V_O], and two V_O, noted T1[2V_O], leading to the formulations $Ba_6Li_2Nb_4O_{17}\square_1$ and $Ba_6Li_2Nb_4O_{16}\square_2$, respectively. In both systems, the oxygen vacancies correspond to Li-V_O-Nb. For T1[2V_O], the charge neutrality was assumed by imposing a homogeneous background charge. Finally, a lowering of symmetry is observed leading to space groups P4mm for these two oxygen vacancy models. It leads to tiny evolutions of the cell parameters, with deviations smaller than 0.6% on the cubic cell parameter. Indeed, the effective cubic cell parameters are both equal to 4.118 Å for T1[1V_O] and T1[2V_O], very close to the experimental value of 4.107 Å. The presence of oxygen vacancies leads to undercoordinated Li, Nb and Ba atoms. All the calculated distances are given in S9.

Figure 8 shows the total densities of states (DOS) of the two T1 models, and the partial DOS projected on the O(2p) and Nb(4d) states.

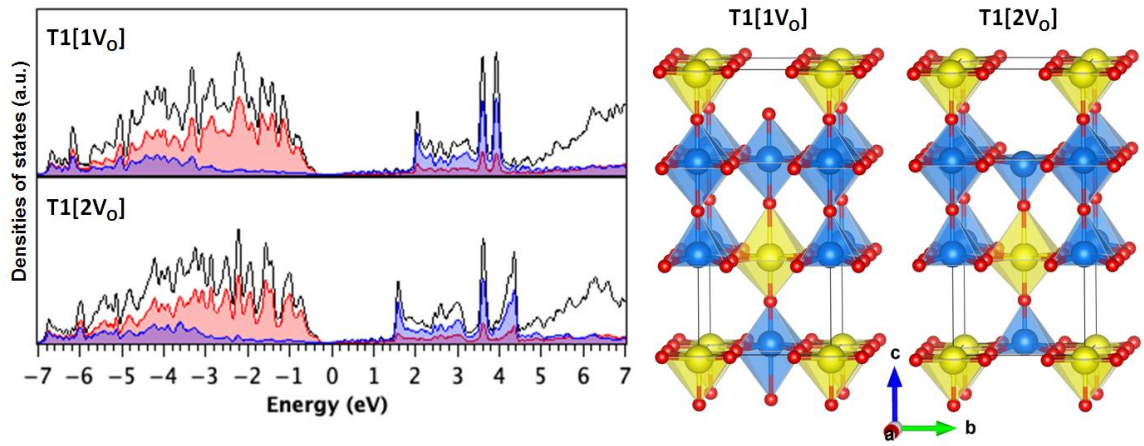

Figure 8 : Densities of states (DOS) of the oxygen vacancy models T1[1V_O] and T1[2V_O] (right) and the related optimized atomic structures (left). Total DOS are represented in black and partial DOS of oxygen and niobium in red and blue, respectively. The Fermi level is defined as the reference of energies. Lithium, niobium and oxygen atoms are represented in yellow, blue, grey and red. The octahedra NbO_6 and LiO_6 are represented in blue and yellow. For simplicity, barium atoms are not represented.

The VB from -7 to 0 eV is mainly composed of O(2p) states interacting with Nb(4d) states. The CB from about 1 to 5 eV is mainly composed of Nb(4d) states interacting with O(2p) states. Adding one more vacancy to the system leads to a band gap reduction of 0.3 eV, i.e. E_g = 0.2 eV. It should be noted that these band gap values are not representative of the optical properties. Indeed, the optical gap could strongly differ from the fundamental one, because it requires allowed dipolar transitions between the occupied and empty states.

In order to get insight into the evolution of the optical properties under heating of the Beige-$O_{8.5}$ sample, we have measured the reflectance spectra of Beige and Pink-$O_{8.5}$. Figure 9a shows the absorption coefficients, deduced from the Kubelka-Munk transformation (KM), as function of the incident energy.

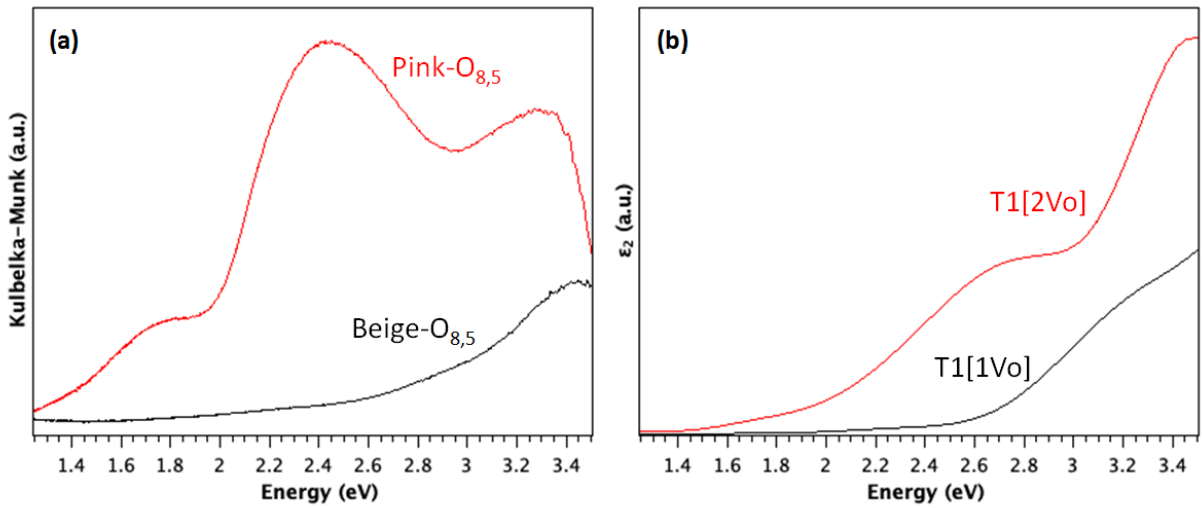

Figure 9 : Experimental (a) and simulated (b) optical properties as function of the photon energy of $Ba_3LiNb_2O_{8.5}\square_{0.5}$. The experimental data corresponds to the absorption coefficient, deduced from the Kubelka-Munk transformation, with Beige and Pink signals in black and red, respectively. The theoretical data corresponds to the imaginary part of the dielectric function, which describe the light absorption, with T1[$1V_O$] and T1[$2V_O$] in black and red, respectively.

Our simulations of the imaginary part of the dielectric function (ε_2) for the 2 models T1[$1V_O$] and T1[$2V_O$] is shown in Figure 9b. ε_2 describes the light absorption and could thus be compared to KM, although the relative intensities are not comparable because the calculation considers a bulk compound while the experiment has been done on powder samples. In addition, the KM absorption coefficient depends not only to absorption processes but although to light extinction due to diffusion processes. We can thus only compare the optical gap values between the present measurements and simulations.

Let's first discuss the KM experimental values. The black curve gives the absorption coefficient of Beige-$O_{8.5}$. It shows an absorption band centred at about 3.4 eV with a tail leading to an optical gap of about 2.8 eV. It explains the beige color which is a mixture of yellow and white. The red curve shows the absorption coefficient of Pink-$O_{8.5}$, which exhibits three peaks centred at about 3.3, 2.4 and 1.7 eV, leading to the pink color which is a mixture of red (due to the largest absorption at 2.4 eV) and white due to the diffusion phenomena related to the pulverulent nature of the samples. In our simulations, T1[$1V_O$] and T1[$2V_O$]

lead to optical gap of about 2.6 and 1.85 eV, respectively. Moreover, the 2 vacancies model shows 2 absorption bands centred at 3.4 and 2.6 eV. Comparing the two simulations, we see an evolution of the optical spectrum which nicely reproduces the experimental data, i.e. appearance of an absorption band inside the visible range and reduction of the band gap value. These features are the consequence of the evolution of the coordination of Nb species, leading to a lift of degeneracy of the Nb(4d) states due to the loss of the ideal octahedral coordination. Indeed, in the proposed core-shell hypothesis, upon heating the oxygen vacancies and Li^+ ions migrate towards the surface, leading to the presence of Li-V_O-Li and Li-V_O-Nb defects which induces highly distorted 6-fold and 5-fold coordinations for the Nb sites inside the shell. PXRD, PND and NMR will not be highly sensitive to such modification of the first layers of the particles. However, the presence of distorted NbO_6 and NbO_5 environments in the shell of the particles will lead to a reduction of the band gap and thus will explain the shift of color from beige to pink upon heating.

We have estimated the quadrupolar coupling frequencies, ν_Q, from the electronic structures calculated by DFT in order to compare with the experimental NMR values for ^{93}Nb. The spectra alone do not contain enough information for a model for the observed disorder; therefore, only an order of magnitude was estimated from the line widths, with a peak ν_Q of 1-2 MHz. In the DFT models without vacancies, i.e. H1, H2 and H3, all Nb are 6-fold coordinated with ν_Q value ranging from -1.6 to 0.4 MHz, leading to an average value of -0.9 MHz. Similarly, the asymmetry parameter η_Q is ranging from 0.00 to 0.04, leading to an average value of 0.01. When incorporating an oxygen vacancy, two types of Nb sites are present in the simulations, with 5-fold and 6-fold coordinations. For the 6-fold coordinated Nb sites the ν_Q values sligthly change with an average value of ν_Q = -0.8 MHz (ranging from -1.8 to 1.4 MHz), while the η_Q significantly deviate from 0, with an average value of η_Q = 0.4 (ranging from 0.0 to 1.0). For the 5-fold coordinated Nb sites, the ν_Q values strongly increase

with an average value of ν_Q = -5.7 MHz (ranging from -6.6 to -4.4 MHz), and the η_Q average value is about 0.2 (ranging from 0.1 to 0.3). Signals with these values would be much broader than those observed experimentally. When taking into account that real signals lose their features by disorder, they will not be detectable and only contribute to the background from the satellite transitions. This would explain that undercoordinated Nb sites were not detected in the NMR spectra (hypothesis 2), in contrast to undercoordinated Li sites.

▪ CONCLUSION

To summarize, a new perovskite phase with the chemical formulation $Ba_3LiNb_2O_{8.5}\square_{0.5}$ has been discovered, with a statistical occupancy of the B site (with 2/3 Nb and 1/3 Li). PXRD and PND data show that this compound crystallises in the Pm-3m space group with a cell parameter of a ≈ 4.108 Å, as the parent $Ba_3Li_{0.75}Nb_{2.25}O_9$ compound. Upon heating at 1400°C in sealed platinum, it undergoes a color change from beige to pink without structure change in contrast to $Ba_3Li_{0.75}Nb_{2.25}O_9$ which remains white and turns to hexagonal. ^{7}Li solid-state NMR reveals undercoordinated lithium environments, due to the oxygen vacancies, while in ^{93}Nb NMR only a decrease of the niobium signal is observed without any sign of a undercoordinated Nb sites. However, DFT calculations show that undercoordinated Nb cations will exhibit enormous quadrupolar coupling which, in conjunction with disorder, impedes their observation by NMR.

A core-shell model is proposed as a possible explanation of the change of color upon heating, due to the migration of both V_O and Li^+ toward the surface of the particles upon heating. The DFT calculations evidence that oxygen vacancies are preferentially formed between two Li^+ ions, if such a situation occurs in the compound, then between Li^+ and Nb^{5+}, and finally between two Nb^{5+} ions. The presence of V_O induces distortions in the NbO_6 octahedra or

undercoordinated NbO_5 environments, leading to lift the degeneracy of the 4d(Nb) states which composed the bottom of the conduction band. It explained the band gap decrease and the color change upon heating. Both Li/Nb distribution and V_O contribute to reduction of the band gap, and will be enhanced by a segregation of the defects at the surface of the particle. It may explain the change of color without observing significant modification of the long-range order which is governed by the core of the particles.

Associated Content

Acknowledgement

The X-ray diffractometer, the TEM and the NMR spectrometer used in this study belong to plateforms of the "Institut des Molécules et Matériaux du Mans (IMMM)": "Plateforme de Diffusion et Diffraction des Rayons-X", "Plateforme de Microscopie Electronique", and "Résonances Magnétiques".

The theoretical calculations were performed using HPC resources from GENCI-[TGCC/CINES/IDRIS] (Grant 2020-A0010907682)

The authors thank Christine Labrugère (PLACAMAT, Université de Bordeaux, UMS 3626, 33600 Pessac, France) for the XPS measurements, Florence Porcher (Laboratoire Léon Brillouin, UMR 12, CEA/CNRS, CEA/Saclay, Gif-sur-Yvette, France), Jérome Lhoste and Amandine Guiet (IMMM, UMR CNRS 6283, Le Mans Université, France) for the optical measurements, Abdel Hadi Kassiba (IMMM, UMR CNRS 6283, Le Mans Université, France) for EPR experiments and valuable discussions, and Emmanuelle Suard (Institut Laue-Langevin, Grenoble, France) for PND data acquisition.

Supporting Information

TEM; Powder X-ray and neutron diffraction patterns; XPS spectra; calculated distances in T1 model and structure refinement results.

Figure captions:

Figure 1: PXRD patterns of $Ba_3Li_{0.75}Nb_{2.25}O_9$ and $Ba_3LiNb_2O_{8.5}\square_{0.5}$ (▼ : K_β) respectively quoted as White-O_9 and Beige-$O_{8.5}$

Figure 2: Observed, calculated and difference PND patterns of Beige-$O_{8.5}$ synthesised at 900°C (S.G.: Pm-3m). Vertical bars are related to the Bragg reflection positions.

Figure 3 : $Ba_3LiNb_2O_{8.5}\square_{0.5}$ before and after the annealing at 1400°C in a sealed platinum tube showing the change in color, Beige-$O_{8.5}$ (left) and Pink-$O_{8.5}$ (right).

Figure 4: NMR spectra of materials White-O_9 (blue), Beige-$O_{8.5}$ (green), and Pink-$O_{8.5}$ (red). (a) ^{7}Li, 40 kHz MAS. (b) ^{93}Nb, 60 kHz MAS. The asterisk denotes the first spinning sideband. (c) ^{93}Nb, static, scaled to the same maximum.

Figure 5: Schematic representation of the optimized geometries of the 3 theoretical models based on a hexagonal supercell (H1, H2 and H3), using meta-GGA SCAN functional. Lithium, niobium, barium and oxygen atoms are represented in yellow, blue, grey and red. The octahedra NbO_6 and LiO_6 are represented in blue and yellow. These three models are without oxygen vacancy and differ by the Li/Nb ordering. The charge neutrality was assumed by imposing a homogeneous background charge.

Figure 6: Densities of states (DOS) of models without oxygen vacancy (left) and simulation of the optical properties of models (right) with or without oxygen vacancy. Total DOS are represented in black and partial DOS of oxygen and niobium in red and blue, respectively. The Fermi level is defined as the reference of energies. The optical properties of the models without oxygen vacancy are shown in grey and the ones with oxygen vacancy in black, blue and red, for an oxygen vacancy Li-V_O-Li, Li-V_O-Nb and Nb-V_O-Nb, respectively.

Figure 7: Relative energies of the models with oxygen vacancy as function of the Li-Li distance. The most stable structure, i.e. H3[1V_O] with an oxygen vacancy between Nb and Li,

has been chosen as the reference of energies. Li-V_O-Li, Li-V_O-Nb and Nb-V_O-Nb correspond to oxygen vacancies between 2 Li, Nb and Li, and 2 Nb atoms, respectively.

Figure 8: Densities of states (DOS) of the oxygen vacancy models T1[$1V_O$] and T1[$2V_O$] (right) and the related optimized atomic structures (left). Total DOS are represented in black and partial DOS of oxygen and niobium in red and blue, respectively. The Fermi level is defined as the reference of energies. Lithium, niobium and oxygen atoms are represented in yellow, blue, grey and red. The octahedra NbO_6 and LiO_6 are represented in blue and yellow. For simplicity, barium atoms are not represented.

Figure 9: Experimental (a) and simulated (b) optical properties as function of the photon energy of $Ba_3LiNb_2O_{8.5}\square_{0.5}$. The experimental data corresponds to the absorption coefficient, deduced from the Kubelka-Munk transformation, with Beige and Pink signals in black and red, respectively. The theoretical data corresponds to the imaginary part of the dielectric function, which describe the light absorption, with T1[$1V_O$] and T1[$2V_O$] in black and red, respectively.

References

1 : Von Hippel, A.; Breckenridge, R.G.; Chesley, F.G.; Tisza, L. High dielectric constant ceramics. *Ind. Eng. Chem.*, **1946,** 38 (11), 1097–1109.

2 : Wu, M.K.; Ashburn, J.R.; Torng, C.J.; Hor, P.H.; Meng, R.L.; Gao, L.; Huang, Z.J.; Wang, Y.Q.; Chu, C.W. Superconductivity at 93 K in a new mixed-phase Y-Ba-Cu-O compound system at ambient pressure *Phys. Rev. Lett.*, **1987**, 58 (9), 908-910.

3 : Von Helmolt, R.; Wecker, J.; Holzapfel, B.; Schultz, L.; Sanwer, K. Giant Negative Magnetoresistance in Perovskite like $La_{2/3}Ba_{1/3}MnO_x$. Ferromagnetic Films *Phys. Rev. Lett*. **1993**,71 (14), 2331-2333.

4 : Galven, C.; Fourquet, J.L.; Crosnier-Lopez, M.P.; Le Berre, F. Mechanism of a reversible CO_2 capture monitored by the layered perovskite $Li_2SrTa_2O_7$ *Dalton Trans*. **2010**, 39, 4191-4197.

5 : Rodzinski, A., Guduru, R., Liang, P. *et al.* Targeted and controlled anticancer drug delivery and release with magnetoelectric nanoparticles. *Sci Reports*. **2016**, 6**,** 20867.

6 : Manser, J.S.; Christians, J.A.; Kamat, P.V. Intriguing Optoelectronic Properties of Metal Halide Perovskites. *Chemical Reviews*. **2016,** 116 (21): 12956-13008.

7 : Mitchell, R.H. Perovskites, Modern and Ancient, Almaz Press, **2002**.

8 : Inaguma, Y.; Liquan, C.; Itoh, M.; Nakamura, T.; Uchida, T.; Ikuta, H.; Wakihara, M. High ionic conductivity in lithium lanthanum titanate *Solid State Com.* **1993**, 86, 10, 689-693.

9 : Colville, A.A.; Geller, S. The crystal structure of brownmillerite Ca_2FeAlO_5. *Acta Cryst*. **1971**, B27, 2311-2315.

10 : Ruddlesden, S.N.; Popper, P. The compound $Sr_3Ti_2O_7$ and its structure. *Acta Cryst.* **1958**, 11, 54-55.

11 : Beznosikov, B.V.; Aleksandrov, K.S. Perovskite-like crystals of Ruddlesden-Popper series. *Cryst. Reports* **2000**, 45, 792-798.

12 : Dion, M. ; Ganne, M. ; Tournoux, M. Nouvelles familles de phases $M^{I}M_2^{II}Nb_3O_{10}$ à feuillets « pérovskites ». *Mater. Res. Bull* **1981**, 16, 1429-1435.

13 : Negas, T.; Roth, R.S.; Parker, H.S.; Brower, W.S. Crystal chemistry of lithium in octahedrally coordinated structures. I. Synthesis of $Ba_8(Me_6Li_2)O_{24}$ (Me = Nb or Ta) and $Ba_{10}(W_6Li_4)O_{30}$. II. The tetragonal bronze phase in the system $BaO\text{-}Nb_2O_5\text{-}Li_2O$ *J. Solid State Chem.* **1973**, 8, 1-13.

14 Collins, B. M.; Jacobson, A. J.; Fender, B. E. F. Preparation of the Ordered Perovskite-Like Compounds $Ba_4M_3LiO_{12}$ (M = Ta,Nb): A Powder Neutron Diffraction Determination of the Structure of $Ba_4Ta_3LiO_{12}$ *J. Solid State Chem.* **1974**, 10, 29-35.

15 : Rice, C.E.; Jackel, J.L.; Rice, C.E.; Jackel, J.L. $HNbO_3$ and $HTaO_3$: New Cubic Perovskites Prepared from LiNbOa and LiTaOa via Ion Exchange *J. Solid State Chem.* **1982**, 41, (3), 308-314.

16 : Rietveld, H. M. A Profile Refinement Method for Nuclear and Magnetic Structures. *J. Appl. Crystallogr.* **1969**, 2 (2), 65–71.

17 : Rodriguez-Carvajal, J. Program FULLPROF Version September 2020, Institut Laue-Langevin, Grenoble.

18 : Albino, M.; Veber, P.; Pechev, S.; Labrugère, C.; Velázquez, M.; Maglione, M.; Josse, M. Growth and Characterization of $Ba_2LnFeNb_4O_{15}$ (Ln = Pr, Nd, Sm, Eu) Relaxor Single Crystals. *Cryst. Growth Des.* **2014**, 14 (2), 500–512.

19 : G. Kresse, G.; Furthmüller, J. Efficiency of ab-initio total energy calculations for metals

and semiconductors using a plane-wave basis set. *Comput. Mater. Sci.* **1996**, *6*, 15–50.

20: Kresse, **G.;** Hafner, J. *Ab initio* molecular-dynamics simulation of the liquid-metal–amorphous-semiconductor transition in germanium**,** *Phys. Rev. B* 1994, *49*, 14251–14269.

21 : G. Kresse, G.; Furthmüller, J. Efficient iterative schemes for *ab initio* total-energy calculations using a plane-wave basis set *Phys. Rev. B* 1996, *54*, 11169–11186.

22 : Perdew, J. P. **;** Burke, K.**;** Ernzerhof, M. Department of Physics, N. O. L. 70118 J. Quantum Theory Group Tulane University, Generalized Gradient Approximation Made Simple**.** *Phys. Rev. Lett.* 1996, *77*, 3865–3868.

23 : Perdew, J. P.; Burke, K.; Ernzerhof, M. Generalized Gradient Approximation Made Simple *Phys. Rev. Lett.* 1997, *78*, 1396–1396.

24 : Blöchl, P. E. The Projector Augmented Wave Method: ab-initio molecular dynamics with full wavefunctions *Phys. Rev. B* **1994**, *50*, 17953–17979.

25 : Kresse, G.; Joubert, D. From ultrasoft pseudopotentials to the projector augmented-wave method *Phys. Rev. B* **1999**, *59*, 1758–1775.

26 : H. J. Monkhorst, J. D. Pack, Special points for Brillouin-zone integrations *Phys. Rev. B* **1976**, *13*, 5188–5192.

27 : Goldschmidt, V.M. Geochemische Verteilungsgesetze der Elemente V11. Skrifter Norske Videnskaps-Akademi, Matematisk-Naturvidenskaplige Klasse, **1926**, Oslo.

28 : Anderson, M.T.; Greenwood, K.B.; Taylor, G.A.; Poeppelmeier, K.R. B-cation arrangements in double perovskites *Progress in Solid State Chem*. **1993**, 22 (3), 197-233.

29 : Shannon, R.D. Revised Effective Ionic Radii and Systematic Studies of Interatomic Distances in Halides and Chalcogenides. *Acta Crystallogr.* **1976**, 32, 751–767.

30 : Brown, I.D.; Altermatt, D. Bond-valence parameters obtained from a systematic analysis of the inorganic crystal structure database *Acta Cryst*. **1985**, B41, 244-247.

31 : Modeshia, D.R.; Walton, R.I.; Mitchell, M.R.; Ashbrook, S.E. Disordered lithium niobate rock-salt materials prepared by hydrothermal synthesis. *Dalton Trans*. **2010**, 39, 6031-6036.

32 : Lapina, O.B.; Khabibulin, D.F.; Romanenko, K.V.; Gan, Z.; Zuev, M.G.; Krasil'nikov, V.N.; Fedorov, V.E. ^{93}Nb NMR chemical shift scale for niobia systems. *Solid State Nucl. Magn. Reson.* **2005**, 28, 204-224.

TOC

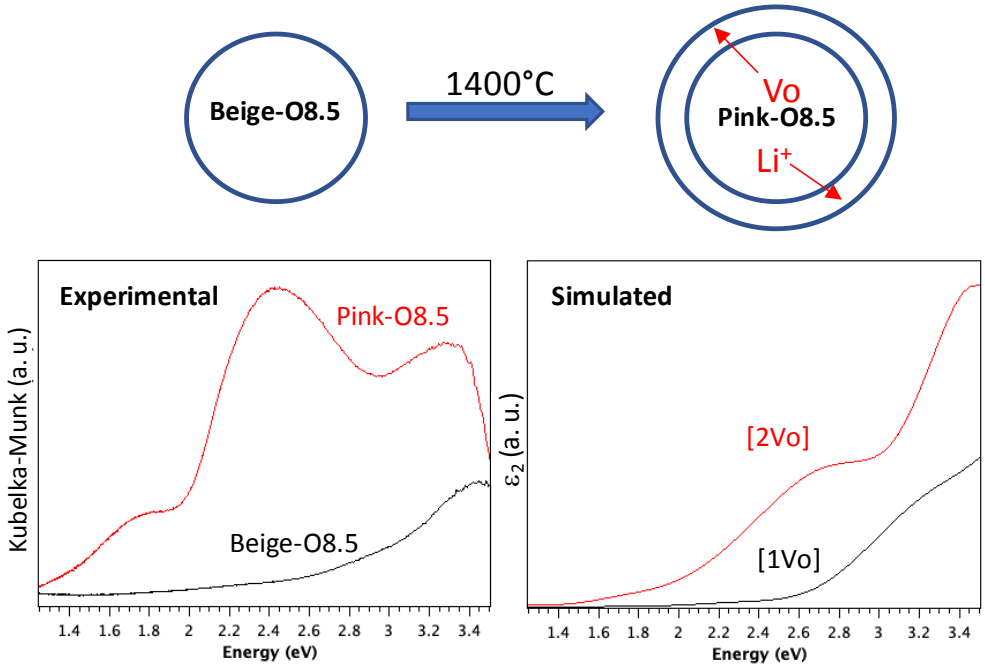

Upon heating, a migration of both V_O and Li^+ toward the surface of the $Ba_3LiNb_2O_{8.5}\square_{0.5}$ particles leads to a color change from beige to pink.